J Mater Sci (2010) 45:6083–6093
DOI 10.1007/s10853-010-4694-y

Microwave-hydrothermal preparation of alkaline-earth-metal tungstates

Kisla P. F. Siqueira · Roberto L. Moreira · Marcelo Valadares · Anderson Dias

Received: 14 February 2010 / Accepted: 3 June 2010 / Published online: 15 June 2010

Abstract Microwave-hydrothermal processing was employed to synthesize nanostructured alkaline-earth-metal tungstate compounds in environmentally friendly conditions not yet found in the literature: 110 °C for times ranging from 5 to 20 min. X-ray diffraction showed that crystalline, single-phase materials were produced, while electron microscopy evidenced nanostructured particles with different morphologies. Raman spectroscopy was used to probe short-range ordering and also to obtain a reliable set of spectra containing all the Raman-active bands predicted by group-theory calculations. The Raman spectra showed no extra feature, indicating that our method gave well-ordered materials without important tetrahedral distortions. Sintered ceramics were submitted to polarized Raman scattering in parallel- and cross-polarized configurations. The E_g modes were totally evidenced in a cross-polarized configuration, while A_g and B_g modes appeared in the parallel arrangement, in complete agreement with the theoretical predictions. Photoluminescence measurements showed broad, complex emission bands, which varied from the blue to the red visible light regions. These results are related to shallow and deep defects into the band gap, through the presence of oxygen vacancies in the complex clusters with metal cations and tungsten atoms.

K. P. F. Siqueira · A. Dias (✉)
Departamento de Química, Universidade Federal de Ouro Preto, Campus Morro do Cruzeiro, ICEB II, Sala 67, Ouro Preto, MG 35400-000, Brazil
e-mail: anderson_dias@iceb.ufop.br

R. L. Moreira · M. Valadares
Departamento de Física, Universidade Federal de Minas Gerais, C.P. 702, Belo Horizonte, MG 30123-970, Brazil

Introduction

Metal tungstates are one of the most studied electro-optical materials because of their excellent properties towards important technological applications: electrochromic devices [1], optical fibers [2], large-scale static displays [3], gas sensors [4], catalysis [5], Raman converters [6], lasers [7], amplifiers [8], and scintillator detectors, including cryogenic phonon scintillation detectors [9]. For chemists, these compounds offer many possibilities for synthesize tailor-made structures, since they can incorporate cations into the host tungstate framework, including combinations and solid solutions with hydrogen, alkaline, and rare-earth elements [10–13]. The result is a huge cast of unique chemical, electrochemical, and electronic properties. Due to the long history of experimental investigations to obtain good materials for practical applications, a very extensive research was devoted to metal tungstates over the past century. Thus, it is difficult to list all the relevant literature on this subject. In an attempt to obtain tailor-made structures, many works reported different techniques and experimental apparatus employed to obtain metal-tungstates: solid-state reactions [14], Czochralski crystal growth [15], electrochemical cells [16], hydrothermal [17], molten salt synthesis [18], solvothermal [19], polymeric precursor technique [20], template-free precipitation [21], reverse-micelle [22], microemulsion [23], sonochemical [24], and microwave-hydrothermal (MW-H) [25]. It is incredible that the number of experimental conditions for each processing route allows the preparation of all types of nanostructures: nanospheres, nanocubes, nanobundles, nanoplates, nanorods, nanowires, nanotubes, and nanoribbons, among others [21, 24, 26–29]. These different morphologies are produced because they could represent ideal structural units for dimension-dependent optical, electrical,

and mechanical properties and, therefore, are particularly attractive building blocks for assembly of functional nanoscale materials [27–29].

Recently, our group has used the microwave energy to synthesize electroceramics with practical interest [30–34]. In these investigations, our goal was to explore the potential of this powerful processing route to obtain tailor-made structures, particularly, needle-like, high anisotropy materials. In this respect, we have employed a microwave apparatus with fully controlled temperature–pressure–time conditions to obtain reliable and reproducible results. Other works appeared in the last 10 years and it is difficult to find investigations that report really controllable conditions during the synthesis of metal tungstates. For the great majority of the papers, the syntheses were conducted in a kitchen-type or a commercially modified kitchen microwave unit. Of course, this technique possesses many advantages among others: use of environmentally friendly solvents; mild processing temperatures, pressures and times; reduced costs associated with heating [35]. However, the indiscriminate use of this technology often produces inconsistent and poorly reproducible results, leading to speculations that there were "nonthermal microwave effects" at work. Since then, the advent of monomode microwaves and multimode instruments with temperature control and monitoring resulted in more consistent results, and the prevailing belief is that nonthermal effects do not exist and are simply the result of uneven microwave dielectric heating.

In this respect, recent works [24, 25, 36–40] reported microwave effects on metal tungstates produced in a commercially modified microwave apparatus, leading to distortions on the tungsten tetrahedra with corresponding generation of extra bands in the Raman spectra, as well as non-linear behavior in photoluminescence as a function of the particle size. The results were interpreted as tetrahedra distortions due to interactions with the microwaves [25, 36]. The currently available microwave technology permits the development and implementation of a temperature–pressure–time-programmed microwave synthesis. In order to investigate and add knowledge on this matter, we have studied the microwave synthesis of alkaline-earth-metal tungstates using a system specifically designed for the requirements of the modern science. The microwave equipment used in this investigation was designed to be corrosion-resistant and with a large interior cavity plasma coated (PTFE) was employed. In this configuration, the microwaves are generated by two magnetrons (800 W each) and distributed into the cavity by a rotating diffuser, thus preventing the localized "hot spots" that can occur in single-magnetron systems with insufficient wave mixing. A maximum power of 1000 W can be used to work in fully controlled temperature–pressure–time conditions, with precise heating and stirring during all processing steps. (Ba,Sr,Ca)WO_4 nanostructured materials were produced at 110 °C, for times from 5 to 20 min, conditions not yet reported in the literature. The goal was to investigate the previously reported distortions in WO_4 tetrahedra using Raman spectroscopy and photoluminescence measurements. Also, field-emission scanning electron microscopy and transmission electron microscopy were employed to characterize the obtained samples. Finally, polarized Raman spectra in sintered tungstate ceramics are reported for the first time, and the active-modes were assigned according to group-theory analysis.

Experimental

$BaWO_4$, $SrWO_4$, and $CaWO_4$ were synthesized using metal nitrates, $Ba(NO_3)_2$, $Sr(NO_3)_2$ and $Ca(NO_3)_2{\cdot}4H_2O$ (>99% Sigma-Aldrich), and sodium tungstate hydrate ($Na_2WO_4{\cdot}2H_2O$, >99% Sigma–Aldrich) as starting materials. The salts were separately dissolved in deionized water and mixed under vigorous stirring. A Milestone BatchSYNTH equipment (2.45 GHz) was employed in the microwave syntheses. The resultant mixed solutions (around 50 mL) presented pH values of 7.9, 7.6, and 7.2, for Ba, Sr, and Ca solutions, respectively. They were put in double-walled digestion vessels (100 mL of capacity) with an inner line and cover made of Teflon Tetrafluormethaxil (TFM) and an outer high strength vessel shell made of Polyether ether keton (PEEK). Following, the system was mounted in a high strength rotor body and secured with a calibrated torque wrench for uniform, isostatical pressure, to prevent leaks and ensure that the pressure-relief spring operates according to the specifications. This equipment operates at a maximum power of 1000 W, where the power can be varied from 0 to 100% controlled by both pressure (autogenous pressure) and temperature (automatic temperature and pressure control). The EasyControl Software was employed to draw a temperature–pressure–time profile, which include a heating time of 2 min up to the processing temperature (110 °C), for times ranging from 5 to 20 min, for the production of the desired materials (the final conditions were 110 ± 1 °C and 1.2 ± 0.2 bar). The magnetic stirring module was used to produce consistent stirring of solutions in all vessels, independent of their position within the cavity. A unique cooling apparatus can be used with segmented rotors to increase air flow during the digestion or when the run is complete. After MW-H syntheses, the products were rinsed with deionized water several times and dried at 80 °C.

X-ray diffraction technique (XRD) was employed to study the structural properties using FeKα radiation ($\lambda = 0.1936$ nm) in a high-resolution Shimadzu D-6000

diffractometer in the range 5–55°2θ (15 s/step of 0.02°2θ), 40 kV, and 20 mA. The results were automatically converted to CuKα radiation for data treatment and manipulation. The precipitated solids were chemically analyzed by inductively coupled plasma (ICP-OES) in Spectra CIROS CCD equipment, which showed that the molar ratios of divalent cation and tungsten in the precipitated samples were in perfect agreement with the theoretical value without impurities. Scanning and transmission electron microscopies were carried out to investigate the morphology of the samples. A Quanta 200 (FEI) field-emission scanning electron microscope (FE-SEM) was employed to analyze the morphology of the tungstate materials (30 kV), while a Tecnai G2-20 (FEI) transmission microscope (TEM) was used to study the morphologies and crystalline aspects of the powders (200 kV). The samples were dispersed in an alcoholic solution and submitted to ultrasound prior to be placed in holey carbon-copper grids (300 mesh). High-resolution TEM (HRTEM) and selected-area electron diffraction (SAED) were obtained in the same Tecnai G2-20 equipment at accelerating voltages of 200 kV. Micro-Raman spectra were collected in back-scattering configuration using an Olympus confocal microscope attached to a Horiba/Jobin–Yvon LABRAM-HR spectrometer (objective 100×), and equipped with 600 and 1800 grooves/mm diffraction gratings. The 632.8 nm line of a He–Ne laser (nominal power of 18 mW) was used as exciting line and a Peltier-cooled charge coupled device (CCD) detected the scattered light. An edge filter was employed to stray light rejection, i.e., the Rayleigh scattered light. Accumulation times of typically 20 collections of 10 s were employed with spectral resolution better than 1 cm^{-1}. All resulting spectra were corrected for the Bose–Einstein thermal factor [41]. Polarized Raman spectra were carried out in samples sintered at 1200 °C, for 8 h. Appropriate interference filter for rejecting laser plasma lines, edge filter for stray light rejection, polarizers and half-wave plate were used. The photoluminescence (PL) spectra were measured in powders at room temperature. A Q-switched Nd:YAG laser emitting at 355 nm (20 mW) was used as the excitation source. The PL emission was focused into an Ocean Optics USB2000 Miniature Spectrometer.

Results and discussion

Figure 1 presents the XRD patterns of $BaWO_4$, $SrWO_4$, and $CaWO_4$ powders processed under MW-H method at 110 °C, for 5 min. These conditions represent the lowest temperature and time ever used to produce metal tungstates under microwaves. As it can be seen, crystalline, single-phase materials were obtained. The XRD patterns were indexed by the scheelite tetragonal $I4_1/a$ structure, space group C_{4h}^6, in agreement with the respective ICDD (International Center of Diffraction Data) cards #43-0646 ($BaWO_4$), #85-0587 ($SrWO_4$), and #77-2234 ($CaWO_4$). XRD data for increasing MW-H times (not shown) are similar, with peaks shifting towards higher angles from Ba to Ca as a result of decreasing ionic radii, as expected. Correspondingly, the lattice parameters decreased in the same order from $BaWO_4$ to $SrWO_4$, and finally $CaWO_4$. The scheelite structure presents, for Ba, Sr, or Ca in combination with WO_4 units, a body-center tetragonal configuration with two formulas per primitive cell ($Z_p = 2$).

The morphologies of the $BaWO_4$, $SrWO_4$, and $CaWO_4$ compounds were examined by FE-SEM and TEM. Figure 2 presents FE-SEM micrographs of samples produced at 110 °C, for 10 min. As it can be seen, different morphologies were obtained depending upon the alkaline-earth-metal used: rice grain-like agglomerates for $BaWO_4$, near spherical-like for $SrWO_4$, and spherically well-dispersed agglomerates, for $CaWO_4$. Similar results for $BaWO_4$ were obtained by Cavalcante et al. [25, 36], although those authors verified an evolution to octahedron-like morphology for longer processing times. For $BaWO_4$, it was observed an anisotropic growth for increasing MW-H times. Figure 3 presents FE-SEM micrographs obtained for $BaWO_4$ samples processed for 5 and 20 min, which show a tendency to aggregate towards faceted-octahedra. Particularly, in the case of $SrWO_4$ and $CaWO_4$, no tendency to form octahedron-like agglomerates was verified.

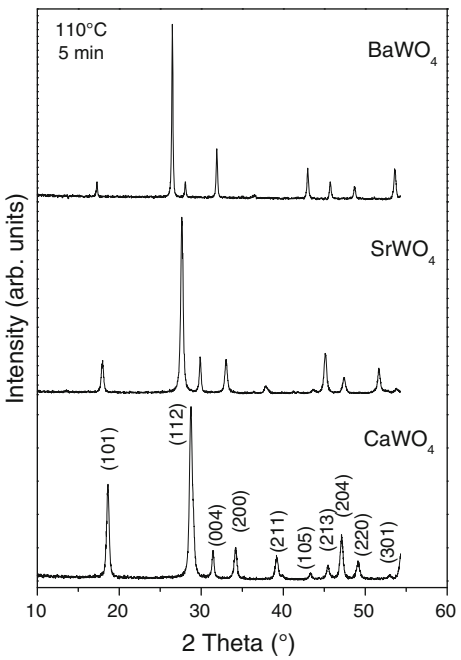

Fig. 1 XRD patterns for the $BaWO_4$, $SrWO_4$, and $CaWO_4$ samples synthesized by microwave-hydrothermal processing at 110 °C, for 5 min

Otherwise, nearly regular agglomerates were identified by TEM. These results are similar to those observed by Thongtem et al. [24]. Figure 4 shows representative TEM (top panel), HRTEM (middle and bottom panels), and SAED (bottom panel) images obtained in $SrWO_4$ samples produced for 5 min (left side) and 20 min (right side) at 110 °C, in which nanosized, well-dispersed particles can be visualized. HRTEM and SAED were taken along a number of selected regions for each individual particle, being indistinguishable from region to region within experimental accuracy for every sample. The presence of two-dimensional lattice fringes clearly illustrate that the particles obtained, even for 5 min, are polycrystalline with little if any defects or dislocations. Interplanar spacings were computed to be about 3.33 Å, for $SrWO_4$ synthesized for 5 min, which corresponds to the (112) planes. For samples produced for 20 min, interplanar spacings of 3.27 and 4.54 Å were identified, which correspond to the (112) and (101) planes, respectively. The associated electron diffraction patterns (insets in the bottom panels) appear as concentric rings, characterized as polycrystals due to the diffraction of electrons through the products. Diffuse rings show that the samples are composed of a number of nanosized crystals with different orientations, which are in agreement with prior observations noted from the XRD patterns for these materials (Fig. 1), corresponding to broad peaks indexed in the scheelite structure.

According to Cavalcante et al. [25, 36], the agglomeration process observed during MW-H synthesis of $BaWO_4$ and $SrWO_4$ could be related to the increase of the collision rates between small particles by the microwave radiation. This agglomeration process would be accelerated also by the polymer surfactant added during synthesis. In our experiments, no surfactant was employed and similar results were observed only for $BaWO_4$ compounds. Therefore, we believe that a different mechanism could be present in the microwave driven synthesis. Reduction in surface energy is the primary driving force for crystal growth and morphology evolution. In the present work, the phenomenon that links particularly all the $BaWO_4$ samples could not be explained by the most cited Ostwald ripening process, in which crystal growth is described in terms of growth of larger particles at the expense of the smaller ones [42]. Microwaves have the useful property of heating some materials, while leaving other cold [43]. Essentially a high-frequency electric field, microwaves cause free ions or electrons to move along the direction of the applied field. Under these conditions, the solvents (water in our case) become superheated and the precipitation (nucleation) occurs rapidly. This fast nucleation leads to the production of very fine particles, which are now free to move according to the applied electromagnetic fields in the microwave reactor. In a second step, the nanostructured particles could undergo a multiplying growth via a "cementing mechanism." Thus, larger particles could be prepared from a direct combination of small crystals, which

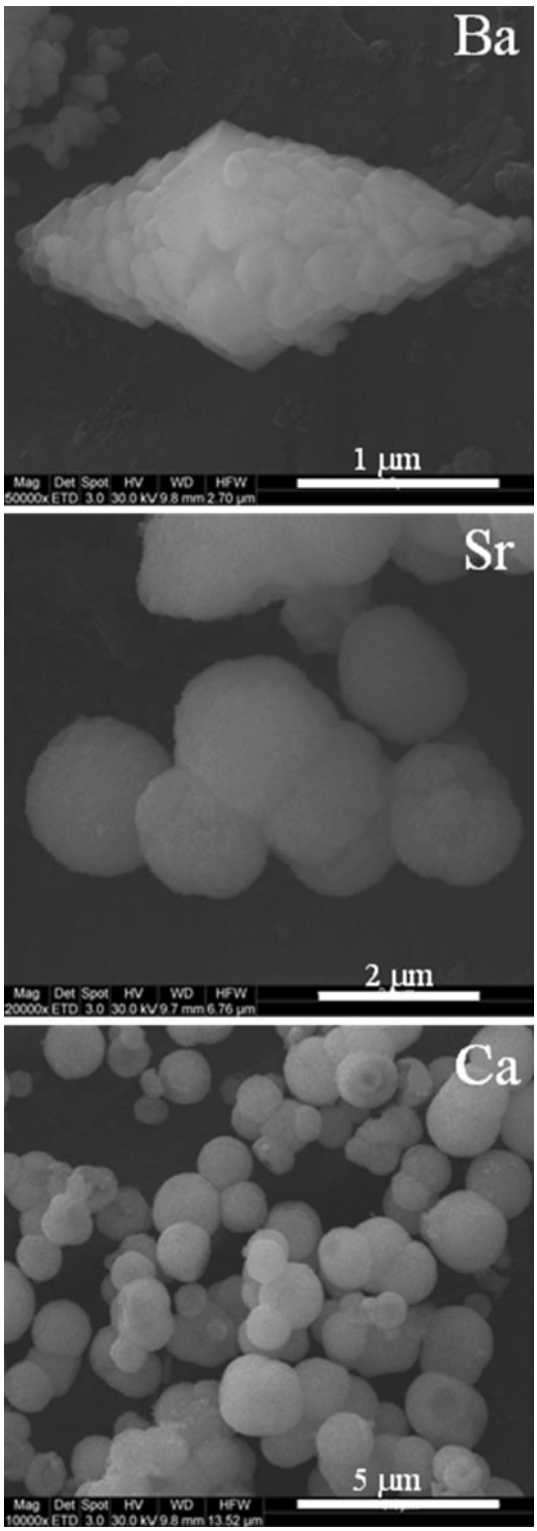

Fig. 2 FE-SEM images for the $BaWO_4$, $SrWO_4$, and $CaWO_4$ samples synthesized by microwave-hydrothermal processing at 110 °C, for 10 min

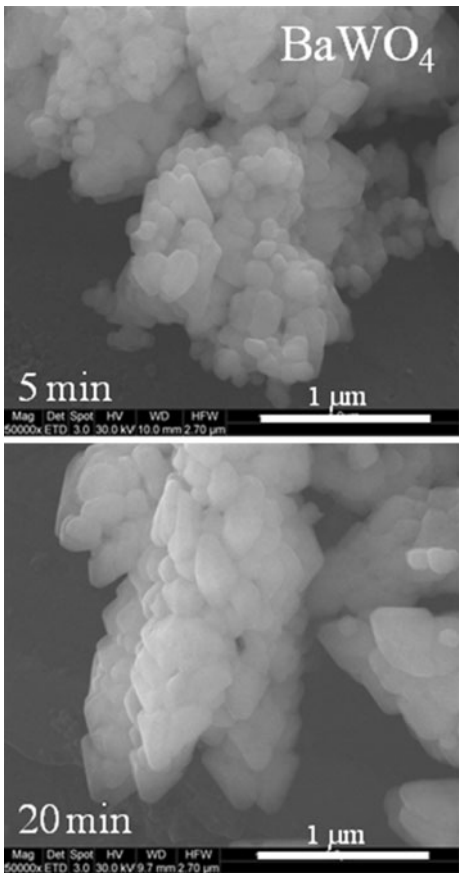

Fig. 3 FE-SEM images for the $BaWO_4$ materials synthesized by microwave-hydrothermal processing at 110 °C, for 5 and 20 min

is also called "oriented attachment" [31, 44]. Under a microwave-hydrothermal condition, the side crystal planes were able to glue together to form larger particles. Thus, we believe that this mechanism involves crystal growth by precise, crystallographically controlled addition of primary individual particles [44]. Similar results were obtained by our research group on complex perovskites [31].

The optical properties of (Ba,Sr,Ca)WO_4 compounds were studied by Raman scattering and photoluminescence (PL). These materials have been described as belonging to the tetragonal $I4_1/a$ (C_{4h}^6) scheelite structure, with $Z_p = 2$ [45]. Thus, they contain 12 atoms in their primitive cell, corresponding to 36 degrees of freedom that can be decomposed in terms of the irreducible representations of the C_{4h} factor group at the Γ-point of the first Brillouin zone, as follows. In the scheelite structure, Ba, Sr, or Ca ions occupy the 4*b* Wyckoff positions of S_4 symmetry, W ions occupy the 4*a* sites of S_4 symmetry and O ions occupy the 16*f* sites with C_1 symmetry. Then, using the site group method of Rousseau et al. [46], we can obtain the following distribution of the degrees of freedom in terms of the irreducible representations (i.r.) of the C_{4h} point group:

$$\Gamma = 3A_g \oplus 5A_u \oplus 5B_g \oplus 3B_u \oplus 5E_g \oplus 5E_u. \quad (1)$$

Once the B_u modes are silent, after subtracting the acoustic modes ($A_u \oplus E_u$), 13 Raman ($3A_g$, $5B_g$, and $5E_g$) and 8 independent infrared ($4A_u$ and $4E_u$) first-order modes are expected.

In the present work, Raman analyses were performed in MW-H powders and sintered ceramics; particularly, polarized Raman spectra were obtained for the first time in sintered samples to discern and assign the active modes. Figure 5 presents the Raman spectra of $BaWO_4$ samples synthesized under microwaves at 110 °C, for 5, 10, 15, and 20 min. As it can be seen, the spectra are very similar without any relevant difference in terms of band frequencies. The linewidth for the A_g mode at 927 cm^{-1} presented a slight decrease for increasing MW-H time: 4.8, 4.1, 4.0, and 3.9 cm^{-1}, for 5, 10, 15, and 20 min, respectively. These results indicate that the MW-H conditions employed, particularly the processing time of 5 min, are sufficient to produce materials with adequate crystallinity and short-range ordering degree. The spectra for all other synthesized compounds ($SrWO_4$ and $CaWO_4$) using identical processing conditions show the same behavior (not shown). The linewidth for the A_g modes at 923 cm^{-1} (Sr) and 915 cm^{-1} (Ca) decreased as a function of the MW-H time (5, 10, 15, and 20 min), as follows: 5.7, 5.4, 5.1, and 5.0 cm^{-1}, for $SrWO_4$, and 8.5, 8.4, 8.2, and 8.2 cm^{-1}, for $CaWO_4$. It is important to note that no extra bands or shoulders were identified. In particular, it was not observed the shoulder verified by Cavalcante et al. [25] in their $CaWO_4$ ceramics at around 830 cm^{-1} and related to distortions in the WO_4 tetrahedra. Those authors attribute such distortions to strong interactions between microwave radiation and tungsten atoms during synthesis. Our results do not corroborate these observations for the processing conditions employed here. We believe that those distortions, if present, could be related to the microwave apparatus employed by Cavalcante et al. [25, 36], which could generate hot-spots or localized heating. Thus, inhomogeneous temperature conditions inside the reactor would lead to unsatisfactory nucleation with production of defective particles.

Figure 6 presents the Raman spectra for samples obtained in extreme conditions: MW-H powders synthesized at 110 °C, for 5 min, and ceramics sintered at 1200 °C, for 8 h. The results show that the sintering process lead to narrower, up-shifted bands in comparison with those observed in MW-H powders because of the higher densities of sintered samples. The linewidths for the A_g modes of the sintered materials at 930 cm^{-1} (Ba), 925 cm^{-1} (Sr), and 916 cm^{-1} (Ca) were 3.8, 4.7, and 8.0 cm^{-1}, respectively. All 13 expected Raman-active bands were identified and their evolution as a function of

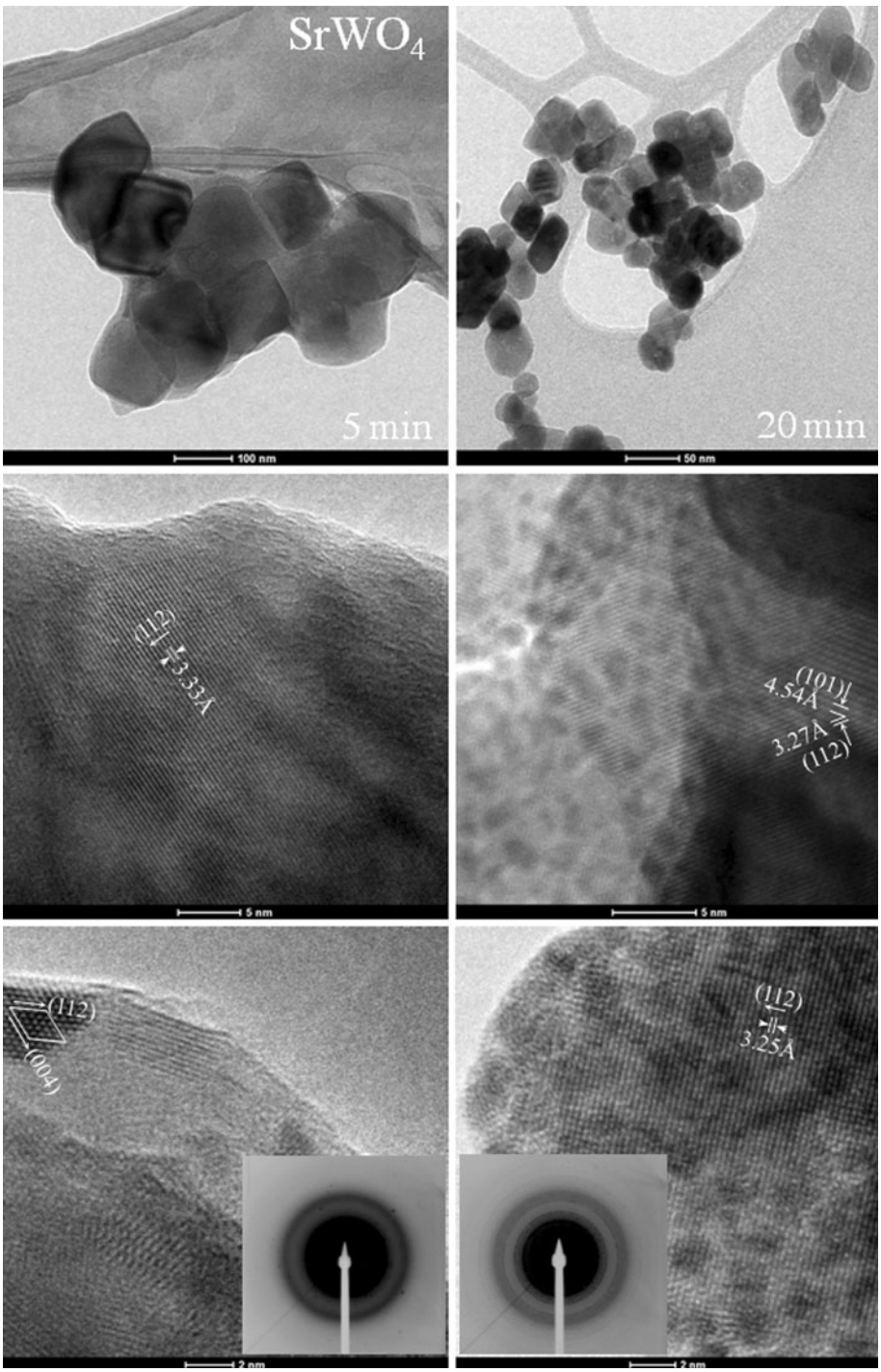

Fig. 4 TEM images for the $SrWO_4$ materials produced at 110 °C for 5 min (*left side*) and 20 min (*right side*). *Top* typical TEM images showing the nanosized particles. *Middle* HRTEM images show lattice fringes and interplanar spacings. *Bottom* HRTEM images in high magnification show interplanar spacings and SAED patterns (*insets*) confirm the polycrystalline nature of the particles

alkaline-earth-metal molecular mass is shown in Fig. 7. In this figure, the symmetries of the modes are tentatively indicated, based on the attribution reported for a $BaWO_4$ single crystal [45–47]. We verify three distinct behaviors of Raman-active mode frequencies with changing metal cations. The first behavior (see Fig. 7) is the monotonously decrease (down-shift) for the most bands as a result of the predominant influence of the cation mass (Ba > Sr > Ca), in particular those modes related to external vibrations (lower frequencies). The second behavior is the fairly decrease verified in some internal modes, apparently not perturbed by cation changes, which could be related by differences in the force constants due to variations in interionic distances. Finally, the relevant increase in the mode frequency (A_g) at around 925 cm^{-1}, which could be related to a size effect or a partially covalent bond between the metal cation (Ba, Sr, or Ca) and the oxygen ions in WO_4^{-2} complexes.

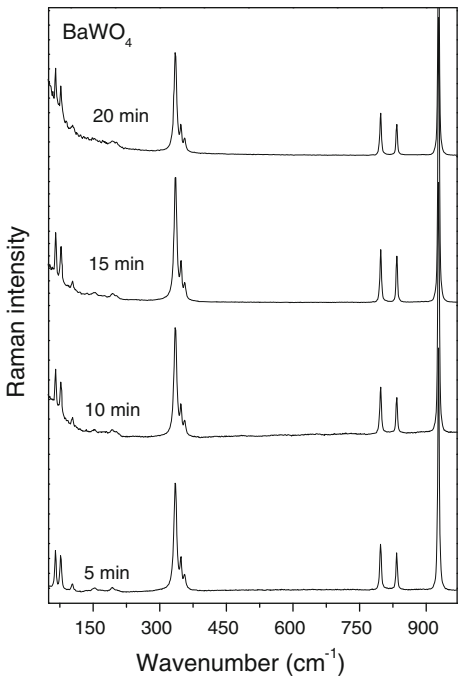

Fig. 5 Raman spectra for $BaWO_4$ MW-H powders obtained at 110 °C for 5, 10, 15, and 20 min

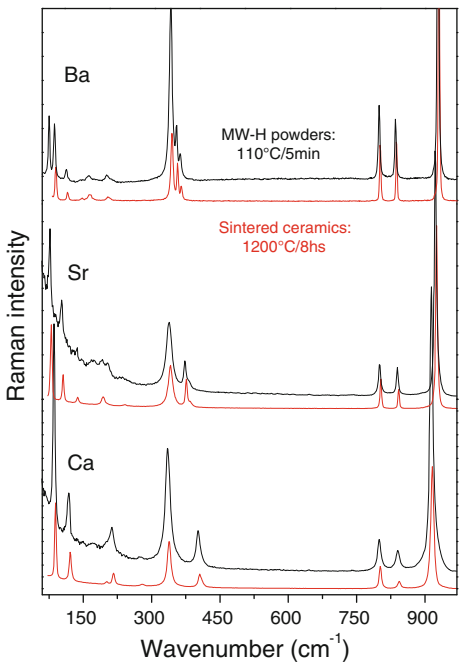

Fig. 6 Raman spectra for the $BaWO_4$, $SrWO_4$, and $CaWO_4$ materials synthesized by microwave-hydrothermal processing at 110 °C, for 5 min (*top black curves*), and sintered at 1200 °C, for 8 h (*bottom red curves*) (Color figure online)

Figure 8 shows the polarized Raman spectra of $BaWO_4$ sintered samples. These results are typical for all the scheelites studied in the present work; however, this sample exhibited the best results for polarized Raman

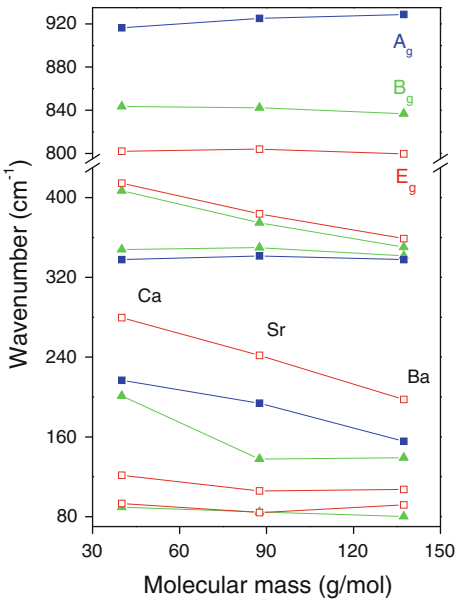

Fig. 7 Raman-frequency evolution as a function of the molecular mass of the alkaline-earth-metal for the sintered ceramics. *Different colors* indicate the different assigned modes: $3A_g$ (*blue*), $5B_g$ (*green*), and $5E_g$ (*red*) (Color figure online)

scattering. This optimized outcome could be related to the bigger grain size (30 μm) if compared with the other compounds (5 μm for $SrWO_4$ and 2 μm for $CaWO_4$). For single crystals, the interesting scattering geometries are $X(ZZ)\bar{X}$, $X(YY)\bar{X}$, $Z(XY)\bar{Z}$, and $X(ZY)\bar{X}$, corresponding to the symmetry species A_g, $(A_g + B_g)$, B_g, and E_g, respectively [45, 47]. It is well-known that the inelastic scattered light intensities due to the Raman effect are proportional to the square of the elements of the polarizability tensor (second-order tensor). Then, the base functions of the irreducible representations that contain the Raman-active modes have a quadratic form, i.e., they transform like the product of the Cartesian coordinates. For single crystals, we take benefit of the crystal symmetry to assign the lattice vibrations to the different irreducible representation [41]. However, in the case of ceramics, although the group theory predictions remain valid, the symmetry of modes is generally mixed due to the random orientation of the crystalline grains.

In our measurements, we have used a confocal microscope with an objective of magnification of 100×, which allows the selection of an observation region as small as 2 μm on the sample surface or even inside the sample. The samples studied here were sintered at 1200 °C for 8 h, which produced grained materials with crystalline grains larger than 2 μm. Nevertheless, we do not know anything about the crystallographic axes of these grains, which have also random orientation throughout the sample. By measuring the micro-Raman spectra of alkaline-earth-metal tungstate materials with cross-polarized light, we displaced

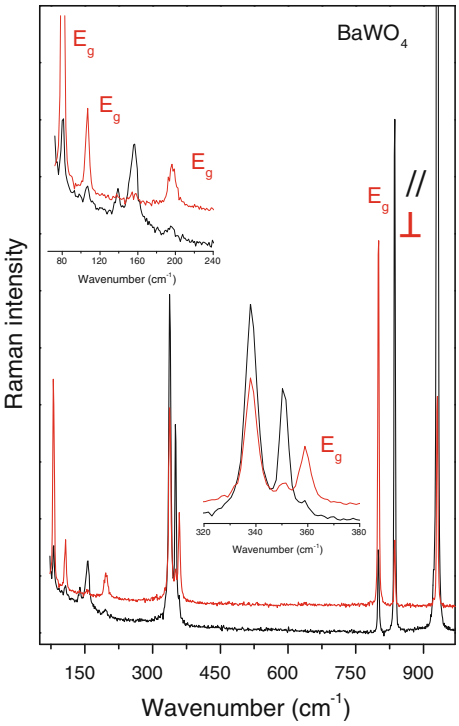

Fig. 8 Polarized Raman scattering for the sintered $BaWO_4$ materials. Parallel- (//) and cross-polarized (⊥) configurations are indicated in black and red lines, respectively. The five E_g modes isolated by the cross-polarized Raman scattering are indicated in *red* (Color figure online)

the sample under the microscope looking for spectral changes. We observed that for some grains the spectra of parallel and crossed light became very different, as exemplified in Fig. 8. For different grains, we always observed the relative strengthening of the bands around 80, 107, 196, 359, and 800 cm^{-1} with cross-polarized light, accompanied by the relative weakening of bands at 68, 139, 156, 338, 351, 839, and 928 cm^{-1}. By observing the variations of the Raman intensities of the mentioned bands at polarized light in different regions of the sample sintered at 1200 °C, we assign them to their respective irreducible representation, in perfect agreement with Ran et al. [45] and Basiev et al. [47]. The first set of five Raman modes (cross-polarized light) can be assigned to the E_g modes, while the other seven bands are designated as B_g, B_g, A_g, B_g (superimposed to one A_g), B_g, B_g, and A_g modes, respectively [45, 47]. The identification of the mode at 338 cm^{-1} is not so simple because its proximity (overlap) with other mode with very near frequency. Ran et al. [45] reported Raman scattering in $BaWO_4$ single-crystals and have a relative success for isolate this mode. The polarization effect visualized in Fig. 8 is undoubtedly due to selection rules linked to the orientation of the grain inside the observation region; particularly, it is noticeable the unambiguous separation of E_g modes in cross-polarized configuration.

PL properties of (Ba,Sr,Ca)WO_4 materials obtained by MW-H processing at 110 °C, for times from 5 to 20 min, were studied at room temperature. The resulting spectra are displayed in Figs. 9, 10, and 11, which show rather broad, complex emission bands. For these compounds, there are many theories in the literature used to explain this complex behavior, which includes charge-transfer transitions within the WO_4^{-2} groups [48], tetrahedra distortions by the influence of Jahn–Teller effect [49], and presence of radiative transitions within defect centers (Frenkel and/or Schottky) [50]. These theories emerge from the different spectra obtained for changing the processing conditions, which could influence the local lattice symmetry (easily probed by PL measurements). In view of this, our samples were studied by PL and each set of samples will be discussed now. Figure 9 presents PL results for $BaWO_4$ samples, which show broad emission bands (at least five bands could be used to fit the spectra after deconvolution with Voigt functions), varying from blue to red visible light for 5 min, with the central peak in the green region. Narrower bands can be seen in the blue region for increasing processing times (10 and 15 min), and finally the central peak shifts again to the green region. Differently from the $BaWO_4$ samples, $SrWO_4$ (Fig. 10) and $CaWO_4$ (Fig. 11) compounds exhibited no red emission bands, but continuous changes from blue to green emissions as a function of MW-H time. However, it is noticeable the broadness of all spectra, which will be discussed below.

Among the theories available in the literature to explain the PL phenomenon in scheelite compounds, it is well-established that the dominant green emission band can be mainly attributed to the charge-transfer transitions within the tungstate tetrahedra groups [50]. However, Figs. 9, 10, and 11 suggest that the emission mechanism in our samples is a multilevel or multiphonon process, in which the relaxation occurs by means of several paths, involving participation of many energy states within the band gap of the material. Thus, our PL data indicate that the emission phenomenon is not a single, isolated phenomenon, but occurs with concurrent phenomena that broadens the emission bands. First, we would like to analyze the recently reported theory that considers tetrahedra distortion promoted by the use of microwaves [25]. In this case, according to Cavalcante et al. [25], the interaction between microwave radiation and tungsten atoms resulted in a rapid heating process and, consequently, significant tetrahedra distortions will be present. The authors verified that these distortions can cause the appearing of extra bands in the Raman spectra, which is an indicative of strong deformations in the short-medium range into the crystals. In our case, these distortions are not present, as showed by the Raman spectra, which presented no extra bands or shoulders. Also, we infer that the results of Cavalcante et al. [25]

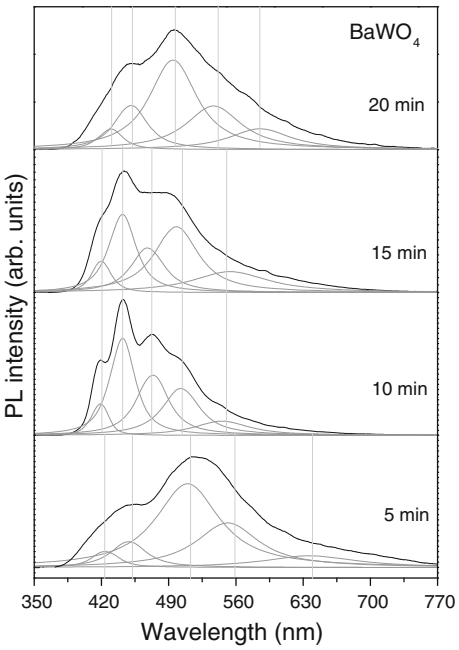

Fig. 9 PL data for the $BaWO_4$ samples synthesized by microwave-hydrothermal processing at 110 °C, for 5, 10, 15, and 20 min. *Gray lines* indicate the emission bands after deconvolution of the complex experimental curve. *Light-gray* vertical lines are guide for the eyes, which show the evolution of emission bands with MW-H time

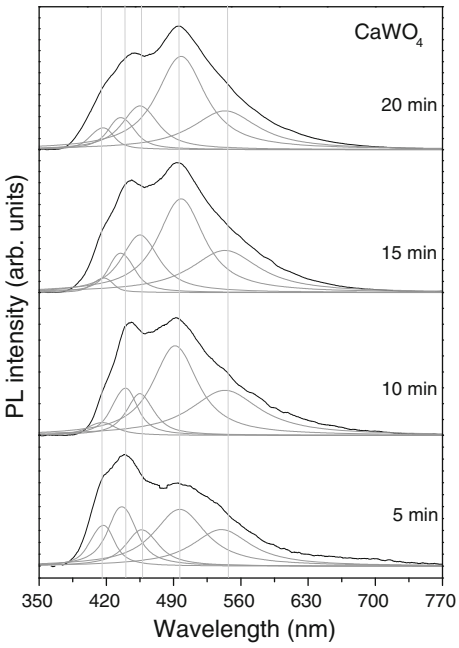

Fig. 11 PL data for the $CaWO_4$ samples synthesized by microwave-hydrothermal processing at 110 °C, for 5, 10, 15, and 20 min. *Gray lines* indicate the emission bands after deconvolution of the complex experimental curve. *Light-gray vertical lines* are guide for the eyes, which show the evolution of emission bands with MW-H time

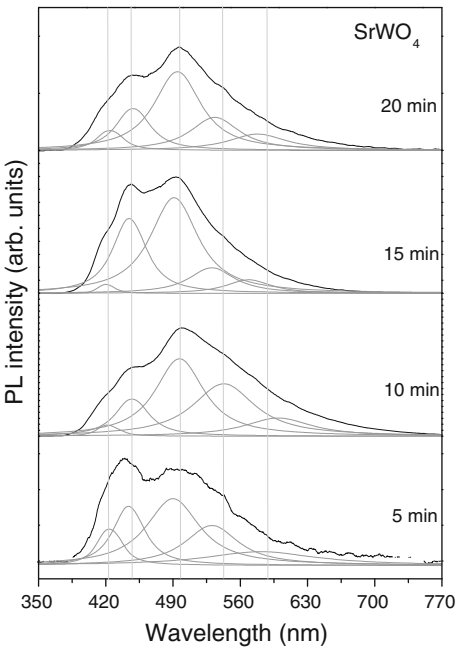

Fig. 10 PL data for the $SrWO_4$ samples synthesized by microwave-hydrothermal processing at 110 °C, for 5, 10, 15, and 20 min. *Gray lines* indicate the emission bands after deconvolution of the complex experimental curve. *Light-gray vertical lines* are guide for the eyes, which show the evolution of emission bands with MW-H time

could be a result of hot-spots during their synthesis because of the equipment used, which would deform the tungsten tetrahedra.

Other theories, including the tetrahedra deformation by Jahn–Teller effect or other electron–phonon interaction, would result in the appearing of defect-activated bands in the Raman spectra [49, 51]. Our spectra are absolutely free of any extra mode, which is a strong indication of well-ordered structures. Thus, the explanation for the very-short range or surface defects evidenced by PL data was based on the previous works of Sinelnikov et al. [52], Lou and Cocivera [53], Laguta et al. [54], more recently, Campos et al. [55], and Longo et al. [56] According to those authors, the controversial blue and red emission bands could be attributed to defect centers associated with oxygen vacancies and intrinsic transitions in the tungsten tetrahedra. The paper of Longo et al. [56] discusses the origins of these emissions in structurally ordered and disordered $CaMoO_4$ samples. For disordered materials, a mechanism based on oxygen vacancies leads to additional levels in the band gap. Our scheelite compounds are formed by WO_4 groups (tungsten is considered the network former), for which oxygen vacancies (*n*-type defects) can be created, $\left[WO_3 \cdot V_O^Z\right]$ in a Kröger–Vink notation, where the complex clusters are formed by neutral or positively charged

species. Similarly, the metal cations are surrounded by eight oxygen atoms into the lattice, which could generate clusters of the type $[BaO_7 \cdot V_O^Z]$. According to band structure calculations, the metal cations ideally tends to bond with eight oxygen atoms, but can show various coordination numbers before this ideal configuration (complex clusters are formed). In this process, new states in the band gap appear as shallow defects. Longo et al. [56] found that localized electronic levels in the band gap are created when these shallow defects are present, which are modulated by the oxygen displacement in the $[BaO_7 \cdot V_O^Z]$ clusters. If disarticulation between the oxygen atoms occurs in the $[WO_3 \cdot V_O^Z]$ clusters, deep defects will emerge and new energy levels are induced in the band gap thus reducing the gap energies [56].

For the samples produced in this work by the MW-H method, two set of materials can be considered. The first set corresponds to the $BaWO_4$ samples, which showed red emission bands for the materials obtained for 5 min. The increase in the processing time lead to materials with blue emission bands (10 and 15 min), followed by a smooth evolution to greenish bands at 20 min. These results showed that $[WO_3 \cdot V_O^Z]$ clusters are probably present in samples obtained for 5 min, leading to a red PL emission (Fig. 9, bottom). These defects disappear for increasing MW-H times and complex $[BaO_7 \cdot V_O^Z]$ clusters linked to shallow defects in the band gap dominate, leading to a more energetic PL emission in the blue wavenumber region (Fig. 9, middle). For these materials, green emission is frequently assumed for a more ordered structure, and is expected to be present in samples obtained in higher temperatures or times. This result was verified in $BaWO_4$ samples obtained for 20 min at 110 °C (Fig. 9, top). As mentioned above, the second set of materials obtained by MW-H processing corresponds to $SrWO_4$ and $CaWO_4$. For these compounds, we found similar PL behavior: a blue dominating emission band for MW-H times up to 10 min, followed by a substantial increase in the green bands for increasing processing times (Figs. 10, 11). These results confirm the presence of $[SrO_7 \cdot V_O^Z]$ and $[CaO_7 \cdot V_O^Z]$ complex clusters (shallow defects) in samples synthesized for 5 and 10 min, and a clear tendency to ordering for increasing times (greenish bands dominate for 15 and 20 min).

Conclusions

Microwave-hydrothermal processing was employed to synthesize nanostructured alkaline-earth-metal tungstate compounds with scheelite structure. The processing conditions were 110 °C, for times ranging from 5 to 20 min, not yet reported in the literature. XRD showed that crystalline, single-phase materials were produced for all the synthesis conditions. Electron microscopy (FE-SEM, TEM, HRTEM, and SAED) showed nanostructured particles with different morphologies, which were function of the alkaline-earth-metal employed. Raman spectroscopy was used to probe short-range ordering and also to obtain a reliable set of spectra containing all the Raman-active bands predicted by group-theory calculations. Polarized Raman scattering was used for the first time in sintered tungstate ceramics at parallel- and cross-polarized configurations. All samples exhibited the same scattering behavior without any extra band. The best results were obtained for $BaWO_4$ materials, which exhibited the higher grain size among all the sintered compounds. The E_g modes were completely evidenced at cross-polarized configuration, while A_g and B_g modes appeared in the parallel arrangement, in complete agreement with the theoretical predictions. PL measurements showed broad, complex emission bands, which could be considered after deconvolution as a sum of five emission bands. These bands varied from the blue to the red visible light regions, which could be attributed to shallow and deep defects related to oxygen complex clusters. These defects generate localized states in the band gap and inhomogeneous charge distribution on the cell, thereby allowing electrons to become trapped. The localized levels are energetically distributed so that different energies are able to excite the trapped electrons.

Acknowledgements The authors acknowledge the financial support from CNPq, FINEP and FAPEMIG. The authors would like to thank the Center of Microscopy—UFMG for technical support with electron microscopy. Special thanks to Prof. Luiz A. Cury (UFMG) for his hospitality during the PL measurements.

References

1. Kuzmin A, Purans J, Kalendarev R, Pailharey D, Mathey Y (2001) Electrochim Acta 46:2233
2. Bradler M, Baum P, Riedle E (2009) Appl Phys B 97:561
3. Hou Z, Li CX, Yang J, Lian HZ, Yang PP, Chai RT, Cheng ZY, Lin J (2009) J Mater Chem 19:2737
4. Sundaram R, Nagaraja KS (2004) Mater Res Bull 39:581
5. Paski E, Blades MW (1988) Anal Chem 60:1224
6. Cerny P, Jelinkova H, Zverev PG, Basiev TT (2004) Prog Quantum Electron 28:113
7. Faure N, Borel C, Couchaud M, Basset G, Templier R, Wyon C (1996) Appl Phys B 63:593
8. Vatnik SM, Maiorov AP, Pavlyuk AA, Plakushchev DV (2001) Quantum Electron 31:19
9. Angloher G, Bruckmayer M, Bucci C, Bühler M, Cooper S, Cozzini C (2002) Astropart Phys 18:43
10. Solodovnikov SF, Mankova OA, Solodovnikova ZA, Ivannikova NV, Alekseev VI (1996) J Struct Chem 37:645
11. Moller T, Clearfield A, Harjula R (2001) Chem Mater 13:4767
12. Gao LH, Lin SK, Sun XJ, Chen JZ (2009) J Rare Earths 27:71
13. Ivleva LI, Basiev TT, Voronina IS, Zverev PG, Osiko VV, Polozkov NM (2003) Optical Mater 23:439

14. Shan ZC, Wang YM, Ding HM, Huang FQ (2009) J Mol Catal A 302:54
15. Jia GH, Tu CY, You ZY, Li JF, Zhu ZJ, Wang Y, Wu BC (2004) J Cryst Growth 273:220
16. Leonova LS, Levchenko AV, Moskvina EI, Tkacheva NS, Aleshina TN, Nadkhina SE, Kolesnikova AM, Dobrovol'skii YA, Bukun NG (2009) Russ J Electrochem 45:593
17. Su YG, Li LP, Li GS (2008) Chem Mater 20:6060
18. Wang YG, Ma JF, Tao JT, Zhu XY, Zhou J, Zhao ZQ, Xie LJ, Tian H (2006) Mater Lett 60:291
19. Hernandez-Sanchez BA, Boyle TJ, Pratt HD, Rodriguez MA, Brewer LN, Dunphy DR (2008) Chem Mater 20:6643
20. Pontes FM, Galhiane MS, Santos LS, Petit LA, Kataoka FP, Mabuchi GH, Longo E, Zampieri M, Pizani PS (2009) J Alloys Compd 477:608
21. Wang XM, Xu HY, Wang H, Yan H (2005) J Cryst Growth 284:254
22. Shi HT, Qi LM, Ma JM, Wu NZ (2005) Adv Functional Mater 15:442
23. He JH, Han M, Shen XP, Xu Z (2008) J Cryst Growth 310: 4581
24. Thongtem T, Phuruangrat A, Thongtem S (2008) Appl Surf Sci 254:7581
25. Cavalcante LS, Sczancoski JC, Lima LF, Espinosa JWM, Pizani PS, Varela JA, Longo E (2009) Cryst Growth Design 9:1002
26. Zhang F, Sfeir MY, Misewich JA, Wong SS (2008) Chem Mater 20:5500
27. Michailovski A, Kiebach R, Bensch W, Grunwaldt JD, Baiker A, Komarneni S, Patzke GR (2007) Chem Mater 19:185
28. Lei S, Tang K, Fang Z, Huang Y, Zhang H (2005) Nanotechnol 16:2407
29. Zhang Q, Chen X, Zhou Y, Zhang G, Yu SH (2007) J Phys Chem C 111:3927
30. Dias A, Ciminelli VST (2003) Chem Mater 15:1344
31. Dias A, Matinaga FM, Moreira RL (2007) Chem Mater 19:2335
32. Moreira RL, Andreeta MRB, Hernandes AC, Dias A (2005) Cryst Growth Design 5:1457
33. Moreira RL, Dias A (2005) J Eur Ceram Soc 25:2843
34. Dias A, Moreira RL (2007) J Phys Chem Solids 68:645
35. Yoshimura M, Byrappa K (2008) J Mater Sci 43:2085. doi: 10.1007/s10853-007-1853-x
36. Sczancoski JC, Cavalcante LS, Joya MR, Espinosa JWM, Pizani PS, Varela JA, Longo E (2009) J Colloid Int Sci 330:227
37. Wang R, Lin C, Zeng J, Li KW, Wang H (2009) J Solid State Chem 182:677
38. Ryu JH, Yoon JW, Lim CS, Oh WC, Shim KB (2005) Ceram Int 31:883
39. Thongtem T, Phuruangrat A, Thongtem S (2008) J Ceram Proc Res 9:258
40. Phuruangrat A, Thongtem T, Thongtem S (2009) J Phys Chem Solids 70:955
41. Hayes W, Loudon R (1978) Scattering of light by crystals. Wiley, New York
42. Baldan A (2002) J Mater Sci 37:2171. doi:10.1023/A:1015388912729
43. Adam D (2003) Nature 421:571
44. Zhang HZ, Banfield JF (2002) Chem Mater 14:4145
45. Ran D, Xia H, Sun S, Zhao P, Liu F, Ling Z, Ge W, Zhang H, Wang J (2006) Cryst Res Technol 41:1189
46. Rousseau DL, Bauman RP, Porto SPS (1981) J Raman Spectrosc 10:253
47. Basiev TT, Sobol AA, Voronko YK, Zverev PG (2000) Optical Mater 15:205
48. Blasse G, Grabmeier BC (1994) Luminescent materials. Springer, Berlin
49. Nikl M, Bohacek P, Mihokova E, Kobayashi M, Ishii M, Usuki Y, Babin V, Stolovich A, Zazubovich S, Bacci M (2000) J Lumin 87–89:1136
50. Grasser R, Scharmann A, Strack K-R (1982) J Lumin 27:263
51. Dias A, Matinaga FM, Moreira RL (2009) J Phys Chem B 113:9749
52. Sinelnikov BM, Sokolenko EV, Zvekova EG (1996) Inorg Mater 32:661
53. Lou Z, Cocivera M (2002) Mater Res Bull 37:1573
54. Laguta VV, Martini M, Vadda A, Rosetta E, Nikl M, Mohokova E, Rosa J, Usuki Y (2003) Phys Rev B 67:205102
55. Campos AB, Simões AZ, Longo E, Varela JA, Longo VM, Figueiredo AT, Vicente FS, Hernandes AC (2007) Appl Phys Lett 91:051923
56. Longo VM, Figueiredo AT, Campos AB, Espinosa JWM, Hernandes AC, Taft CA, Sambrano JR, Varela JA, Longo E (2008) J Phys Chem A 112:8920